

1  
2  
3  
4  
5  
6  
7  
8  
9  
10  
11  
12  
13  
14  
15  
16  
17  
18  
19  
20  
21  
22

**A change in the relation between the Subtropical Indian Ocean Dipole and the  
South Atlantic Ocean Dipole indices in the past four decades**

Lejiang Yu<sup>1\*</sup>, Shiyuan Zhong<sup>2</sup>, Timo Vihma<sup>3</sup>, Cuijuan Sui<sup>4</sup>, and Bo Sun<sup>1</sup>

1 MNR Key Laboratory for Polar Science, Polar Research Institute of China,  
Shanghai, China,

2 Department of Geography, Environment and Spatial Sciences, Michigan State  
University, East Lansing, MI, USA,

3 Finnish Meteorological Institute, Helsinki, Finland

4 National Marine Environmental Forecasting Center, Beijing, China

\*Corresponding Author's address Dr. Lejiang Yu

MNR Key Laboratory for Polar Science, Polar Research Institute of China, Shanghai,  
China

Jinqiao Road 451, 200136, Shanghai, China

Phone: 0086-020-58712034, email: yulejiang@sina.com.cn

## 23 **Abstract**

24 We utilized the global atmospheric reanalysis (ERA5) and reconstructed sea  
25 surface temperature (SST) data from 1979 through 2020 to examine the stability of  
26 the relationship between the SST oscillations in the southern Indian and the Atlantic  
27 Oceans described by the Subtropical Indian Ocean Dipole (SIOD) and the South  
28 Atlantic Ocean Dipole (SAOD) indices. We note a significant positive correlation  
29 between the two indices prior to the year 2000 but practically no correlation  
30 afterwards. We show that in the two decades prior to 2000, a positive phase of SAOD  
31 is associated with more convective activities over the subtropical southern Atlantic  
32 Ocean and eastern Brazil, which trigger a stronger upper-atmosphere wavetrain, and  
33 further produces stronger southern subtropical highs and surface anti-cyclonic  
34 circulations and therefore a stronger correlation between the two indices. The  
35 situation is reversed after 2000. Our results are potentially applicable for predictions  
36 of precipitation in southern Africa and South America.

## 37 **1 Introduction**

38 A southwest-northeast-oriented dipole mode characterizes the anomalous sea  
39 surface temperature (SST) patterns over the subtropical South Indian and Atlantic  
40 Oceans (Wang, 2010). The former is referred to as the Subtropical Indian Ocean  
41 Dipole (SIOD) mode (Behera and Yamagata, 2001) and the latter is named as the  
42 South Atlantic Ocean Dipole (SAOD) mode (Venegas et al., 1997). The two  
43 subtropical modes display similar seasonal variability with their peaks in austral  
44 summer (Morioka et al., 2012). Surface latent heat flux anomalies play a vital role in

45 their variability (Sterl and Hazeleger, 2003; Suzuki et al., 2004; Hermes and Reason,  
46 2005). Moreover, the interannual variability of the two modes has been linked to the  
47 El Niño–Southern Oscillation (ENSO) (Boschat et al., 2013). The two subtropical  
48 modes exert a great influence on precipitation in Africa and South America (Reason,  
49 2001; 2002; Vigaud et al., 2009; Nnamchi and Li, 2011; Morioka et al., 2012; Wainer  
50 et al., 2020) and, therefore, understanding the relationship between the two modes has  
51 practical implications for precipitation forecasts in Africa and South America on  
52 seasonal scale and beyond.

53 Using observational data, Fauchereau et al. (2003) noted the co-variability of the  
54 SIOD and SAOD indices in austral summer. Hermes and Reason (2005) confirmed  
55 the co-variability of the two indices and attributed it to an anomalous subtropical high.  
56 Both studies suggested a linkage between the two indices and an atmospheric zonal  
57 wavenumber-4 pattern in the Southern Hemisphere. Lin (2019) also suggested the  
58 atmospheric zonal wavenumber-4 pattern controlling the South Atlantic–South Indian  
59 Ocean SST pattern. The atmospheric wavenumber-4 was also observed in other  
60 studies (Chiswell, 2021; Senapati, et al., 2021). The global wave-number-4 pattern in  
61 SST includes southern subtropical Indian and Atlantic Ocean components that  
62 resemble the two subtropical dipole modes (Senapati et al., 2021). The linkage  
63 between the SST patterns in the Southern Hemisphere ocean basins and their relation  
64 with atmospheric wavenumber-4 pattern is a challenging and active research topic  
65 worthy of further investigation.

66 Although previous studies have suggested that a relationship exists between the

67 SIOD and the SAOD indices, few have focused on the stability of the relationship. In  
68 this study, we examine the SIOD-SAOD relationship over the past four decades from  
69 1979 through 2020. We underscore a change in the relationship that occurred around  
70 2000 and provide a physical explanation for the change.

## 71 **2 Datasets and methods**

72 Monthly SST data from the United States National Oceanic and Atmospheric  
73 Administration (NOAA) Extended Reconstructed SST V5 (Huang et al., 2017) is the  
74 primary dataset ~~are~~ utilized to calculate the SIOD and SAOD indices. A secondary  
75 SST data, ~~To confirm the results, we also use~~ the Kaplan Extended SST V2 data set  
76 from the UK Met Office (Kaplan et al., 1998), is also used to confirm the results.  
77 Following previous studies, we derive the SIOD index as the difference in the SST  
78 anomalies between the western (55-65 °E, 37-27 °S) and eastern (90-100 °E, 28-18 °S)  
79 subtropical Indian Ocean (Behera and Yamagata, 2001) and the SAOD index as the  
80 difference of SST anomalies between the south-western (10-30 °W, 30-40 °S) and  
81 north-eastern (0-20 °W, 15-25 °S) South Atlantic Ocean (Morioka et al., 2011).

82 Atmospheric data from the European Centre for Medium-Range Weather Forecasts  
83 (ECMWF) fifth-generation reanalysis (ERA5, Hersbach et al., 2020) provide the  
84 upper-level (200-hPa) and surface atmospheric variables used in our analyses except  
85 for the. ~~We also employ~~ monthly top-of-atmosphere (TOA) outgoing longwave  
86 radiation (OLR) that is from the NOAA Interpolated OLR dataset (Liebmann and  
87 Smith, 1996). For SST or atmospheric variables, the anomalies refer to the departure  
88 from their climatology computed as the 42-year averaged value.

89 Correlation and regression analyses are utilized to examine the relationship  
90 between the SIOD and the SAOD indices. The confidence levels are determined by  
91 the two-tailed Student's t test. Before the correlation or regression analyses are  
92 applied to the data, the variables and indices are detrended. We also remove the  
93 influence from the ENSO signal using the method proposed by An (2003), where the  
94 ENSO signal is represented by the Niño 3.4 index. The generation and propagation of  
95 planetary waves are identified on the basis of the Rossby wave source (RWS) and the  
96 wave activity flux (WAF). The RWS is calculated following Sardeshmukh and  
97 Hoskins (1988) and the WAF is derived using the method of Takaya and Nakamura  
98 (2001). Notice that due to the peak of the SIOD and SAOD in February (Morioka et  
99 al., 2012), the austral seasons in this study refer to summer (January-March), autumn  
100 (April-June), winter (July-September), and spring (October-December).

### 101 **3 Results**

102 The ~~regressed spatial patterns of temporal anomalies of SST depicted by~~ SIOD  
103 and SAOD indices ~~on detrended SST anomalies~~ display southwest-northeast-oriented  
104 dipoles in the subtropical southern Indian Ocean (~~SIOD~~, Figure 1a) and Atlantic  
105 Ocean (~~SAOD~~, Figure 1b). ~~Using the NOAA Extended Reconstructed SST V5 data,~~  
106 ~~†~~The correlations between the SIOD and SAOD indices over the 42-year period are  
107 0.56 for austral summer ( $p < 0.05$ ), becoming insignificant in other seasons with  
108 correlation coefficients dropping by nearly half to 0.23 for austral autumn and winter  
109 and 0.25 for austral spring. Removing the ENSO signal resulted in small changes in  
110 the correlations and their seasonal variations, with summer being the only season

111 when the two indices are significantly correlated (0.45,  $p < 0.01$ ) (Figure 1c). The  
112 Kaplan Extended SST V2 data yielded similar results, with slightly lower  
113 summertime correlation coefficients ~~of:~~ 0.49 (with ENSO signal) and 0.38 (without  
114 ENSO signal,  $p < 0.05$ ). Henceforth, we focus on the summer time series without the  
115 ENSO signal.

116 To assess the stability of the SIOD-SAOD correlation over the past four decades,  
117 we calculate moving correlation of the two indices using 15-year and 20-year sliding  
118 windows (Figure 1d). For the 15-year window, the correlation is above (below) the 95%  
119 confidence level before (after) 1998 and for the 20-year sliding window the shifting  
120 occurs in 2003. Similar results are obtained using the Kaplan Extended SST V2 data  
121 (Figure 2). There is a remarkable difference in the correlation between the two indices  
122 prior to and after 1999 (Figure 1d). For the 1979-1999 period, the correlation  
123 coefficient is 0.64 ( $p < 0.01$ ), dropping sharply to only 0.19 ( $p > 0.05$ ) for the 2000-2020  
124 period. Results derived using the Kaplan Extended SST V2 data are ~~almost very~~  
125 similar, with the correlation coefficients of 0.60 ( $p < 0.01$ ) for the 1979-1999 period  
126 and 0.20 ( $p > 0.05$ ) for the 2000-2020 period. This notable drop in the correlation  
127 between the SIOD and SAOD indices from the first two decades to the next two  
128 warrants further investigation. Below we explore the reasons behind the change.

129 We compare the regression maps of the Southern Hemisphere SST anomalies on  
130 the summertime SAOD and SIOD indices for the 1979-1999 period with those for the  
131 2000-2020 period (Figure 3). There are clear differences in the anomalous SST  
132 patterns between the two periods. As a response to the positive phase of the SAOD

133 index, significant SST anomalies occur in the southern subtropical Indian Ocean  
134 during the 1979-1999 period, with a spatial pattern (Figure 3a) closely resembling the  
135 positive phase SIOD index (Figure 1a); however, the SST anomalies for the  
136 2000-2020 period are not significant in the southern subtropical Indian Ocean (Figure  
137 3b). Similarly, corresponding to the SIOD index, a dipole of significant SST  
138 anomalies appears in the South Atlantic Ocean (Figure 3c) for the 1979-1999 period  
139 that bear strong resemblance to the positive phase SAOD pattern (Figure 1b), whereas  
140 for the 2000-2020 period, the SST anomalies are insignificant (Figure 3d). These  
141 results confirm the strong correlation between the SAOD and SIOD indices during the  
142 first two decades and the lack of correlation in the last two decades, separated by the  
143 turn of the century. The SST anomalies in Figure 3 display the appearance of the SST  
144 wavenumber-4 mode (Senapati et al., 2021), including the SIOD and SAOD pattern.  
145 Senapati et al. (2022) suggested that the weakening of the SST wavenumber-4 pattern  
146 after 2000 is related to South Pacific Meridional Mode. In addition, ~~after 2000, the~~  
147 weaker SIOD-SAOD relationship after 2000 ~~is due~~ may be related to the decadal  
148 variability of a warm pool dipole, with opposite SST anomalies in the southeastern  
149 Indian Ocean and the western-central tropical Pacific Ocean (Zhang et al., 2021).

150 Lin (2019) related a South Atlantic-South Indian Ocean pattern to a wavetrain  
151 induced by the South Atlantic Convergence Zone anomaly. We hypothesize that the  
152 stability of the SAOD-SIOD relation may also be related to the strength of the  
153 wavetrain. To test this hypothesis, we examine the regression patterns of several  
154 atmospheric variables related to convective and wave activities (OLR, RWS, WAF,

155 | 200-hPa divergent wind, and streamfunction); to the SAOD index in austral summer  
156 | separately for the 1979-1999 period and the 2000-2020 period (Figure 4). Over the  
157 | 1979-1999 period, corresponding to the positive phase of the SAOD index,  
158 | convective activities are enhanced over the southern subtropical Atlantic Ocean and  
159 | eastern Brazil, which are flanked by suppressed convective activities over tropical and  
160 | mid-latitude South Atlantic Ocean (Figure 4a). The convective activities over western  
161 | subtropical southern Atlantic Ocean and eastern Brazil produce positive RWS and  
162 | 200-hPa divergent wind (Figure 4c), which trigger a wavetrain propagating  
163 | southeastwards into the South Atlantic Ocean, and then eastwards into the South  
164 | Indian Ocean, Australia and the South Pacific Ocean (Figure 4e). The wavetrain  
165 | generates negative streamfunction anomalies over the South Indian and Atlantic  
166 | Oceans (Figure 4e). In contrast, over the 2000-2020 period, the magnitude of the  
167 | anomalous OLR is less significant than that over the 1979-1999 period (Figure 4b).  
168 | Weaker RWS and upper level divergent wind (Figure 4d) indicate a weaker wavetrain,  
169 | which results in weaker streamfunction anomalies over the South Atlantic and Indian  
170 | Oceans (Figure 4f).

171 | Although the magnitudes of the [SST-OLR](#) anomalies related to the SAOD index  
172 | are comparable over the two periods (Figure 4a and 4b), the anomalous OLR and  
173 | RWS and the related wavetrain associated with the SAOD index are substantially  
174 | different between the two periods. The differences in the climatological conditions  
175 | over the two periods may provide a plausible explanation. For example, over the  
176 | subtropical southern Atlantic Ocean and most of Brazil, [the climatological](#) OLR



177 anomalies are generally negative during the 1979-1999 period, suggesting stronger  
178 convective activity favorable for the generation of the wavetrain (Figure 5a), but in  
179 contrast, OLR anomalies are mostly positive during 2000-2020, indicating suppressed  
180 convective activities unfavorable for the formation of the wavetrain (Figure 5b). Thus,  
181 the interdecadal variability of the OLR activities can modulate the effect of the SAOD  
182 mode on atmospheric circulation patterns over other ocean basins.

183 The SAOD and SIOD modes are related to the subtropical highs in the South  
184 Atlantic and Indian Oceans, with stronger high corresponding to the positive phase of  
185 the two indices due to wind-induced evaporation (Wang, 2010; Behera and Yamagata,  
186 2001; Venegas et al., 1997). We proceed to examine the climatological mean sea level  
187 pressure and surface wind field related to the aforementioned wavetrain over the two  
188 periods (Figure 6). The position and strength of the climatological subtropical highs  
189 and the associated surface winds in the southern Indian and the Atlantic Oceans show  
190 little difference over the two periods (Figure 6a and 6b). However, the regression of  
191 the mean sea level pressure to the SAOD index for the two periods show considerably  
192 stronger subtropical highs and anti-cyclonic circulations in the South Atlantic and the  
193 Indian Oceans over the 1979-1999 period than the 2000-2020 period (Figure 6c and  
194 6d). According to the study of Hermes and Reason (2005), a stronger subtropical high  
195 favors larger magnitude of the SST anomalies represented by the SAOD and SIOD  
196 indices. The large decrease in the strength of the summertime subtropical high  
197 associated with SAOD from the first two decades to the next two (Figure 6c, 6d)  
198 corroborates the sharp drop in the SAOD-SIOD correlation (Figure 1d).

199 Similarly, we have also obtained the patterns of the aforementioned atmospheric  
200 circulation variables associated with the SIOD index separately for the two periods  
201 (Figure 7). During 1979-1999, ~~the anomalous OLR, RWS and 200 hPa divergent~~  
202 ~~wind fields favor the causal chain for the wavetrain generation, negative OLR~~  
203 ~~anomalies occurs~~ over the northern South America, corresponding to upper-level  
204 ~~divergent wind and positive RWS anomalies, while positive OLR anomalies exist~~  
205 ~~over the southern Atlantic Ocean, leading to upper-level c~~onvergent wind and  
206 ~~negative RWS anomalies (Figure 7a and 7c). Those anomalous RWSs produce an~~  
207 ~~anomalous a~~-Rossby wavetrain propagating from the southern Atlantic Ocean to  
208 ~~southern Indian Ocean (Figure 7e). but this is not the case during 2000-2020. During~~  
209 ~~2000-2020, negative (positive) OLR anomalies over the tropical (subtropical) central~~  
210 ~~Pacific Ocean and positive OLR anomalies over the subtropical central Pacific Ocean~~  
211 ~~generate anomalous upper-level winds and RWSs, which excite a wavetrain~~  
212 ~~propagating from the Pacific to South America and the southwestern South Atlantic~~  
213 ~~Ocean (Figure 7b, 7d, and 7f). Meanwhile, stronger convective activities over the~~  
214 ~~southwestern Indian Ocean and weaker convective activities over central Indian~~  
215 ~~Ocean also produce anomalous RWSs, which triggers a local wavetrain propagating~~  
216 ~~eastwards into Australia. However, the two wavetrains are controlled by different~~  
217 ~~factors and are not connected to~~with each other over the South Atlantic Ocean.

218 We also examine the MSLP and surface wind field related to the SIOD index in  
219 austral summer for the 1979-1999 and 2000-2020 periods (Figure 8). Over the  
220 1979-1999 period, there is two-stronger subtropical highs develop over the South

221 Indian and Atlantic Oceans, which induce the positive phase of the SIOD and SAOD  
222 modes, respectively (Figure 8a), suggesting that the SIOD and SAOD index is  
223 connected ~~to~~with each other through the aforementioned wavetrain (Figure 7e). Over  
224 the 2000-2020 period, positive MSLP anomalies and anomalous anticyclonic  
225 circulation dominate over the South Indian Ocean, though negative MSLP anomalies  
226 and anomalous cyclonic circulation occur over the southwestern South Indian Ocean  
227 (Figure 8b). The atmospheric circulation anomalies over the South Indian Ocean ~~are~~is  
228 related to the OLR anomalies and induced ~~a~~ local wavetrain (Figure 7b, 7d and 7f).  
229 The positive MSLP anomalies and anticyclonic circulation anomalies ~~do not occur~~are  
230 absent over the South Atlantic Ocean (Figure 8b). ~~Above~~These results indicate that  
231 the SIOD mode over the 2000-2020 period is related to local convective activities, not  
232 to those over the South Atlantic Ocean.

233 ~~The SAOD and SIOD modes are related to the subtropical highs in the South~~  
234 ~~Atlantic and Indian Oceans, with stronger high corresponding to the positive phase of~~  
235 ~~the two indices due to wind-induced evaporation (Wang, 2010; Behera and Yamagata,~~  
236 ~~2001; Venegas et al., 1997). We proceed to examine the climatological mean sea level~~  
237 ~~pressure and surface wind field related to the aforementioned wavetrain over the two~~  
238 ~~periods (Figure 7). The position and strength of the climatological subtropical highs~~  
239 ~~and the associated surface winds in the southern Indian and the Atlantic Oceans show~~  
240 ~~little difference over the two periods (Figure 7a and 7b). However, the regression of~~  
241 ~~the mean sea level pressure to the SAOD index for the two periods show considerably~~  
242 ~~stronger subtropical highs and anti-cyclonic circulations in the South Atlantic and the~~

243 ~~Indian Oceans over the 1979–1999 period than the 2000–2020 period (Figure 7c and~~  
244 ~~7d). According to the study of Hermes and Reason (2005), a stronger subtropical high~~  
245 ~~favors larger magnitude of the SST anomalies represented by the SAOD and SIOD~~  
246 ~~indices. The large decrease in the strength of the summertime subtropical high~~  
247 ~~associated with SAOD from the first two decades to the next two (Figure 7c, 7d)~~  
248 ~~corroborates the sharp drop in the SAOD–SIOD correlation (Figure 1d).~~

#### 249 **4 Conclusion and discussion**

250 In this study, we examined the relation between the oscillations of the SST in the  
251 subtropical South Indian and the Atlantic Oceans described by the SIOD and SAOD  
252 indices and the stability of the relation using the ERA5 global atmospheric reanalysis  
253 and reconstructed SST data from 1979 through 2020. We found significant relation  
254 between the two indices in austral summer. Through moving correlation analyses, we  
255 discovered that the relation in austral summer was not stable for the past four decades.  
256 Specifically, the correlation between the two indices was significant prior to 2000 but  
257 insignificant afterwards. The change in the relation between the two indices is  
258 attributed to a change in the strength of the atmospheric wavetrain induced by  
259 anomalous convective activity over the subtropical southern Atlantic Ocean and  
260 eastern Brazil. More frequent and stronger convective activities prior to 2000 excited  
261 stronger wavetrain, which produced stronger subtropical highs during the positive  
262 phase of SAOD, resulting in a stronger relation between the two indices. The opposite  
263 occurred after 2000.

264 The interdecadal variability of OLR over the subtropical South America and

265 Atlantic Ocean is [the](#) key to the relation between the SAOD and SIOD indices. What  
266 determined the OLR anomalies in the region prior to and after 2000 needs to be  
267 further investigated. Hermes and Reason (2005) suggested that the southern  
268 subtropical high is related to the Antarctic Oscillation (AAO) and the linkage  
269 strengthened after mid-1970s. The influence of the change in the AAO index on the  
270 relation between the SAOD and the SIOD indices needs to be assessed. Yu et al.  
271 (2017) noted a phase change of the Atlantic Multidecadal Oscillation (AMO) and the  
272 Pacific Decadal Oscillation (PDO) indices in the late 1990s, with PDO shifting from  
273 positive to negative and AMO switching from negative to positive around 1999. Dong  
274 and Dai (2015) noted the influence of IPO on precipitation in Brazil. However, the  
275 influence from the same phase of the IPO has great uncertainty and depends on the  
276 period and dataset (Dong and Dai, 2015). Jones and Carvalho (2018) suggested more  
277 precipitation in Brazil during the negative phase of the AMO than during its positive  
278 phase. Longer datasets are utilized to examine the effect of the IPO and AMO on  
279 convective activity over the subtropical South America and Atlantic Ocean on the  
280 interdecadal time scale. Although our results are only based on statistical analyses,  
281 they have potential for improving the prediction of precipitation in southern Africa  
282 and South America.

### 283 *Data Availability*

284 The monthly SST data from the U.S. NOAA Extended Reconstructed Sea Surface  
285 Temperature (ERSST) version 5 (ERSST v5) are available online  
286 (<https://www1.ncdc.noaa.gov/pub/data/cmb/ersst/v5/netcdf/>). Kaplan Extended SST

287 V2 data are derived from below website  
288 ([https://psl.noaa.gov/cgi-bin/db\\_search/DBSearch.pl?Dataset=Kaplan+Extended+SST](https://psl.noaa.gov/cgi-bin/db_search/DBSearch.pl?Dataset=Kaplan+Extended+SST+V2&Variable=Sea+Surface+Temperature)  
289 [+V2&Variable=Sea+Surface+Temperature](https://psl.noaa.gov/cgi-bin/db_search/DBSearch.pl?Dataset=Kaplan+Extended+SST+V2&Variable=Sea+Surface+Temperature)). The monthly ERA5 reanalysis data are  
290 available from the Copernicus Climate Data Store  
291 (<https://www.ecmwf.int/en/forecasts/datasets/reanalysis-datasets/era5>). The monthly  
292 OLR data are derived from the NOAA Interpolated OLR  
293 ([https://psl.noaa.gov/cgi-bin/db\\_search/DBSearch.pl?Dataset=NOAA+Interpolated+O](https://psl.noaa.gov/cgi-bin/db_search/DBSearch.pl?Dataset=NOAA+Interpolated+OLR&Variable=Outgoing+Longwave+Radiation)  
294 [LR&Variable=Outgoing+Longwave+Radiation](https://psl.noaa.gov/cgi-bin/db_search/DBSearch.pl?Dataset=NOAA+Interpolated+OLR&Variable=Outgoing+Longwave+Radiation)).

#### 295 *Acknowledgments*

296 We thank the European Centre for Medium-Range Weather Forecasts (ECMWF) for  
297 the ERA5 data. This study is financially supported by the National Key R&D  
298 Program of China (2022YFE0106300), the National Science Foundation of China  
299 (41941009), and the European Commission H2020 project Polar Regions in the Earth  
300 System (PolarRES; Grant101003590).

301 *Author contributions.* LY designed the research, analyzed the data, and wrote the first  
302 draft of the paper. S Z and TV revised the first draft and provided useful insights  
303 during various stages of the work. CS and BS provided some comments and helped  
304 with editing the paper.

305 *Competing interests.* The authors declare that they have no conflict of interest.

#### 306 **References**

307 An, S. I.: Conditional maximum covariance analysis and its application to the  
308 tropical Indian Ocean SST and surface wind stress anomalies, *J. Climate*, 16,  
309 2932–2938, 2003.

310 Behera, S. K., and Yamagata, T.: Subtropical SST dipole events in the southern  
311 Indian Ocean, *Geophys. Res. Lett.*, 28, 327-331, 2001.

312 Boschat, G, Terray, P., and Masson, S.: Extratropical forcing of ENSO, *Geophys. Res.*  
313 *Lett.*, 40, 1605-1611, 2013.

314 Chiswell, S. M.: Atmospheric wavenumber-4 driven South Pacific marine heat waves  
315 and marine cool spells, *Nature Communication*, 12, 4779, 2021.

316 Dong, B., and Dai, A.: (2015).The influence of the Interdecadal Pacific Oscillation on  
317 temperature and precipitation over the global, *Clim. Dyn.*, 45, 2667-2681.

318 Fauchereau, N., Trzaska, S., Richard, Y., Roucou, P., and Camberlin, P.: Sea  
319 Surface temperature co-variability in the Southern Atlantic and Indian Oceans  
320 And its connections with the atmospheric circulation in the Southern  
321 Hemisphere, *Int. J. Climatol.*, 23, 663–677, 2003.

322 Hermes, J. C., and Reason, C. J. C.: Ocean model diagnosis of interannual coevolving  
323 SST variability in the South Indian and South Atlantic Oceans, *J. Climate*, 18,  
324 2864-2882, 2005.

325 Hersbach, H., Bell, B., Berrisford, P., Hirahara, S., Horányi, A., Muñoz-Sabater, J.,  
326 Nicolas, J., Peubey, C., Radu, R., Schepers, D., Simmons, A., Soci, C., Abdalla,  
327 S., Abellan, X., Balsamo, G., Bechtold, P., Biavati, G., Bidlot, J., Bonavita, M.,  
328 De Chiara, G., Dahlgren, P., Dee, D., Diamantakis, M., Dragani, R., Flemming,  
329 J., Forbes, R., Fuentes, M., Geer, A., Haimberger, L., Healy, S., Hogan, J. R.,  
330 Hólm, E., Janisková, M., Keeley, S., Laloyaux, P., Lopez, P., Lupu, C., Radnoti,  
331 G., de Rosnay, P. Rozum, I., Vamborg, F., Villaume, S., and Thépaut J.-N.: The  
332 ERA5 global reanalysis, *Quarterly Journal of the Royal Meteorological Society*,  
333 146, 1999-2049, 2020.

334 Huang, B., Thorne, P. W., Banzon, V. F., and Zhang, H. M.: Extended Reconstructed  
335 SeaSurface Temperature version 5 (ERSSTv5), Upgrades, validations, and  
336 Intercomparisons, *J. Climate*, 30, 8179-8205, 2017.

337 Jones, C., and Carvalho, L. M. V.: The influence of the Atlantic multidecadal  
338 oscillation on the eastern Andes low-level jet and precipitation in South  
339 America, *npj Climate and Atmospheric Science*, 1, 40, 2018.

340 Kaplan, A., Cane, M., Kushnir, Y., Clement, A., Blumenthal, M., and Rajagopalan, B.:  
341 Analyses of global sea surface temperature 1856-1991, *J. Geophys. Res.*, 103,  
342 18567-18589, 1998.

343 Liebmann, B., and Simth, C. A.: Description of a complete (interpolated)  
344 outgoing longwave radiation dataset, *Bulletin of the American Meteorological*  
345 *Society*, 77, 1275–1277, 1996.

346 Morioka, Y., Tozuka, T., and Yamagata, T.: On the growth and decay of the  
347 subtropical dipole mode in the south Atlantic. *J. Climate*, 24, 5538-5554, 2011.

348 Morioka, Y., Tozuka, T., Masson, S., Terray, P., Luo, J.-J., and Yamagata, T.:  
349 Subtropical dipole modes simulated in a coupled general circulation mode, *J.*  
350 *Climate*, 25, 4029-4047, 2012.

351 Nnamchi, H. C., and Li, J. P.: Influence of the South Atlantic Ocean Dipole on West  
352 African summer precipitation, *J. Climate*, 24, 1184-1197, 2011.

353 Reason, C. J. C.: Subtropical Indian Ocean SST dipole events and southern  
354 African rainfall, *Geophys. Res. Lett.*, 28, 2225–2227, 2001.

355 Reason, C. J. C.: Sensitivity of the southern African circulation to dipole sea-surface  
356 temperature patterns in the South Indian Ocean, *Int. J. Climatol.*, 22, 377–393,  
357 2002.

358 Sardeshmukh, P. D., and Hoskins, B. J.: The generation of global rotational flow  
359 by steady idealized tropical divergence, *J. Atmos. Sci.*, 45, 1228–1251, 1988.

360 Senapati, B., Deb, P., Dash, M. K., and Behera, S. K.: Origin and dynamics of  
361 global atmospheric wavenumber-4 in the Southern mid-latitude during austral  
362 summer. *Climate Dynamics*, doi:10.1007/s00382-021-06040-z, 2021.

363 Senapati, B., Dash, M. K., and Behera, S. K.: Global wave number-4 pattern in  
364 the southern subtropical sea surface temperature, *Scientific Reports*, 11, 142,  
365 doi:10.1038/s41598-020-80492-x, 2021.

366 [Senapati, B., Dash, M. K., and Behera, S. K.: Decadal variability of southern](#)  
367 [subtropical SST wavenumber-4 pattern and its impact. \*Geophysical Research\*](#)  
368 [Letters](#), e2022GL099046. doi:10.1029/2022GL099046, 2022.

369 Sterl, A., and Hazeleger, W.: Coupled variability and air-sea interaction in the



370 South Atlantic Ocean. *Climate Dyn.*, 21, 559–571, 2003.

371 Suzuki, R., Behera, S. K., Iizuka, S., and Yamagata, T.: Indian Ocean Subtropical dipoles  
372 simulated using a coupled general circulation model. *J. Geophys. Res.*, 109,  
373 C09001, doi:10.1029/2003JC001974, 2004.

374 Takaya, K., and Nakamura, H.: A formulation of a phase in dependent wave-activity  
375 flux for stationary and migratory quasi geostrophic eddies on a zonally varying  
376 basic flow. *J. Atmos. Sci.*, 58, 608–627, 2001.

377 Vigaud, N., Richard, Y., Rouault, M., and Fauchereau, N.: Moisture transport between  
378 The South Atlantic Ocean and southern Africa: Relationships with summer  
379 rainfall and associated dynamics. *Climate Dyn.*, 32, 113–123, 2009.

380 Venegas, S. A., Mysak, L. A., and Straub, D. N.: Atmosphere–ocean coupled  
381 variability in the South Atlantic, *J. Climate*, 10, 2904–2920, 1997.

382 Wainer, I., Prado, L. F., Khodri, M., and Otto-Bliesner, B.: The South Atlantic  
383 subtropical dipole mode since the last deglaciation and changes in rainfall,  
384 *Climate Dynamics*, 56, 109–122, doi:10.1007/s00382-020-05468-z, 2020.

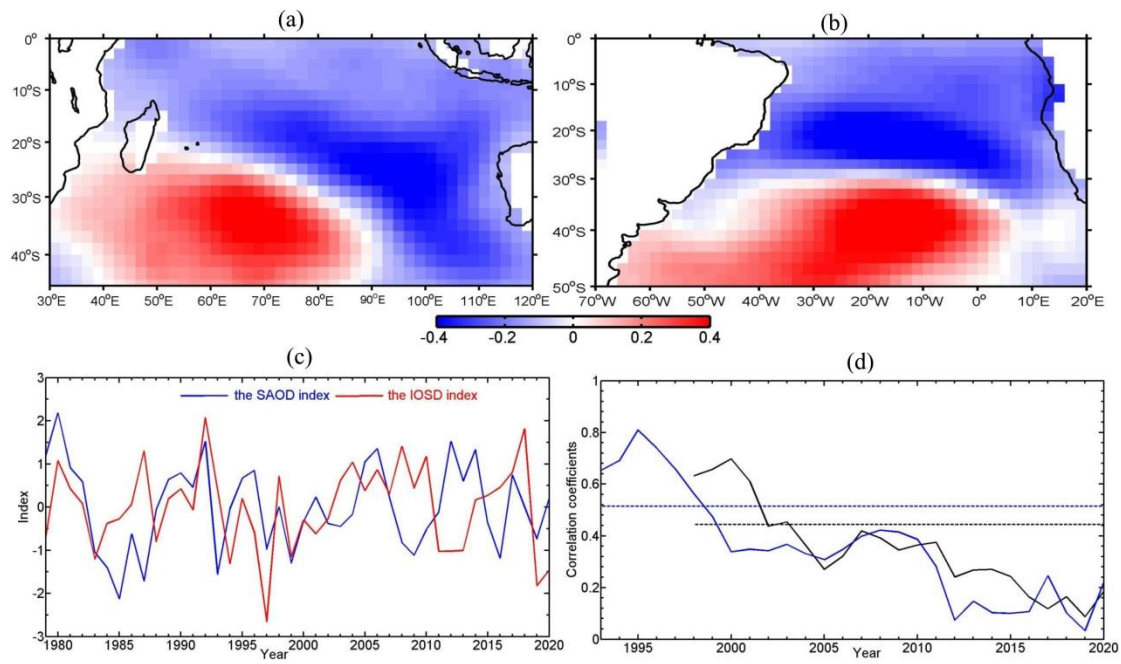
385 Wang, F.: Subtropical dipole mode in the Southern Hemisphere: A global view.  
386 *Geophys. Res. Lett.*, 37, L10702, doi:10.1029/2010GL042750, 2010.

387 Yu, L., Zhong, S., Winkler, J. A., Zhou, M., Lenschow, D. H., Li, B., Wang, X., and  
388 Yang, Q.: Possible connection of the opposite trends in Arctic and Antarctic  
389 sea ice cover. *Scientific Reports*, 7, 45804, 2017.

390 [Zhang, L., Han, W., Karnauskas, K. B., Li, Y., and Tozuka, T.: Eastward shift of](#)  
391 [Interannual climate variability in the South Indian Ocean since 1950.](#)  
392 [Journal of Climate, 35, 561–575.](#)

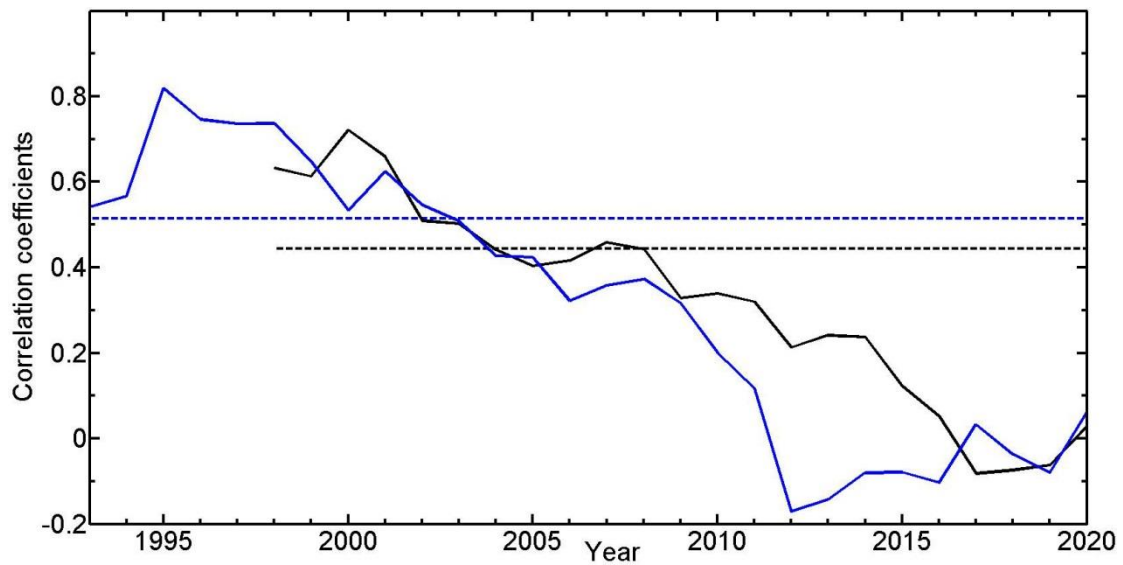
393

394



395  
 396  
 397  
 398  
 399  
 400  
 401  
 402  
 403  
 404  
 405  
 406

Figure 1. Spatial-Regression patterns of austral summer (JFM) SST anomalies ( $^{\circ}\text{C}$ ) for-on the positive phase of the summertime indices of (a) the Subtropical Indian Ocean Dipole (SIOD), (b) the South Atlantic Ocean Dipole (SAOD), and (c) their time coefficients, and as well as (d) the moving correlations between the detrended and ENSO-signal-removed SIOD and SAOD indices (time coefficients) using athe 20-year (black solid line) and a 15-year (blue solid line) sliding window (~~black solid line~~) and 15-year sliding window (~~blue solid line~~). In (d), the dashed lines denote the correlation coefficients with the 95% confidence level for 20 ~~samples~~ (black ~~line~~) and 15 ~~samples~~ (blue ~~line~~) samples and the abscissa indicates the end year of the moving correlations. The above results are derived using the NOAA Extended Reconstructed SST V5 data.



408

409 Figure 2 Moving correlations of the detrended and ENSO-signal-removed SIOSD and SAOD  
 410 indices using the 20-year (black solid line) and a 15-year (blue solid line) sliding window. ~~(black~~  
 411 ~~solid line) and 15-year sliding window (blue solid line) (d).~~ ~~The two indices are removed from the~~  
 412 ~~ENSO signal and their trends.~~ Dashed lines denote the correlation coefficients with the 95%  
 413 confidence level for 20 ~~samples~~ (black ~~line~~) and 15 ~~samples~~ (blue ~~line~~) ~~samples~~. Abscissa  
 414 indicates the end year of the moving correlations. The above results are obtained using the  
 415 Kaplan Extended SST V2 data.

416

417

418

419

420

421

422

423

424

425

426

427

428

429

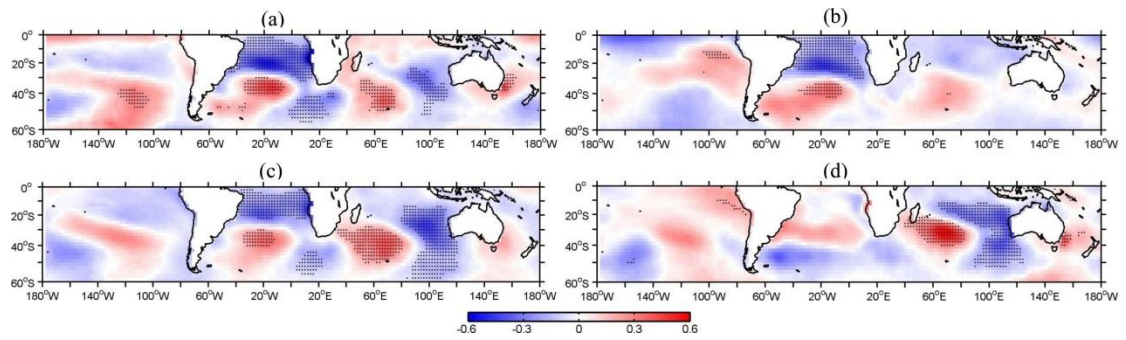
430

431

432

433

434



435

436

Figure 3. Regression maps of the SST anomalies ( $^{\circ}\text{C}$ ) onto the summertime indices of (a), (b) SAOD and (c), (d) SIOD, over the periods of (a), (c) 1979-1999 and (b), (d) 2000-2020. Dots denote the regions of above 95% confidence level.

439

440

441

442

443

444

445

446

447

448

449

450

451

452

453

454

455

456

457

458

459

460

461

462

463

464

465

466

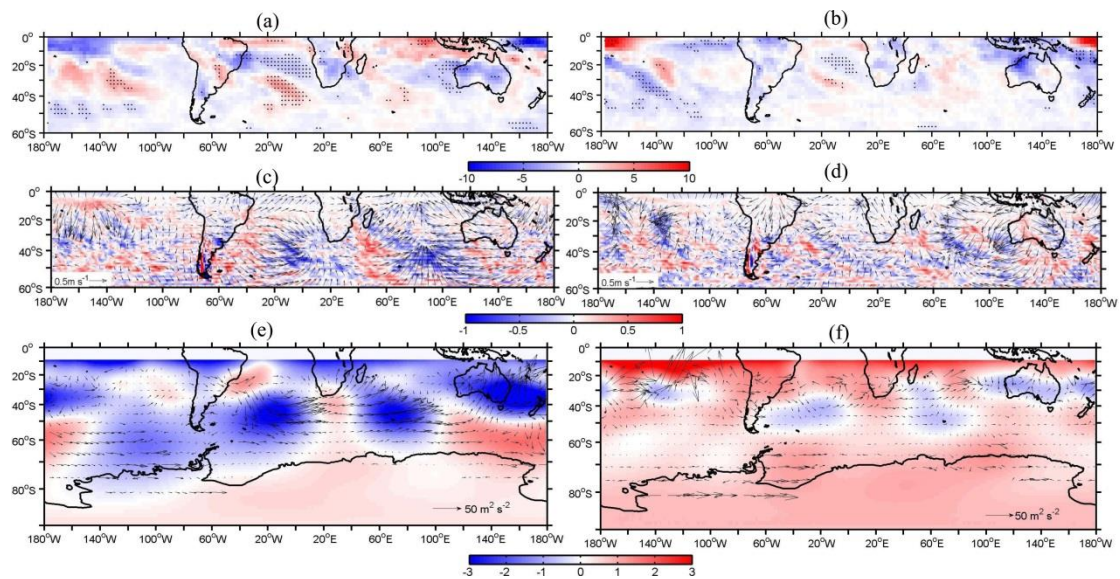
467

468

469

470

471



472

473

474 | Figure 4. Regression maps of (a), (b) the anomalous outgoing longwave radiation (OLR) ( $\text{W m}^{-2}$ )  
 475 | at the top of the atmosphere, (c), (d) Rossby wave source (RWS) ( $10^{-10} \text{s}^{-2}$ ) and 200-hPa divergent  
 476 | wind (vector), and (e), (f) wave activity flux (WAF) (vector) and streamfunction ( $\text{m}^2 \text{s}^{-1}$ ) onto the  
 477 | summertime SAOD index over the periods of (a), (c), (e) 1979-1999 and (b), (d), (f) 2000-2020.

478

479

480

481

482

483

484

485

486

487

488

489

490

491

492

493

494

495

496

497

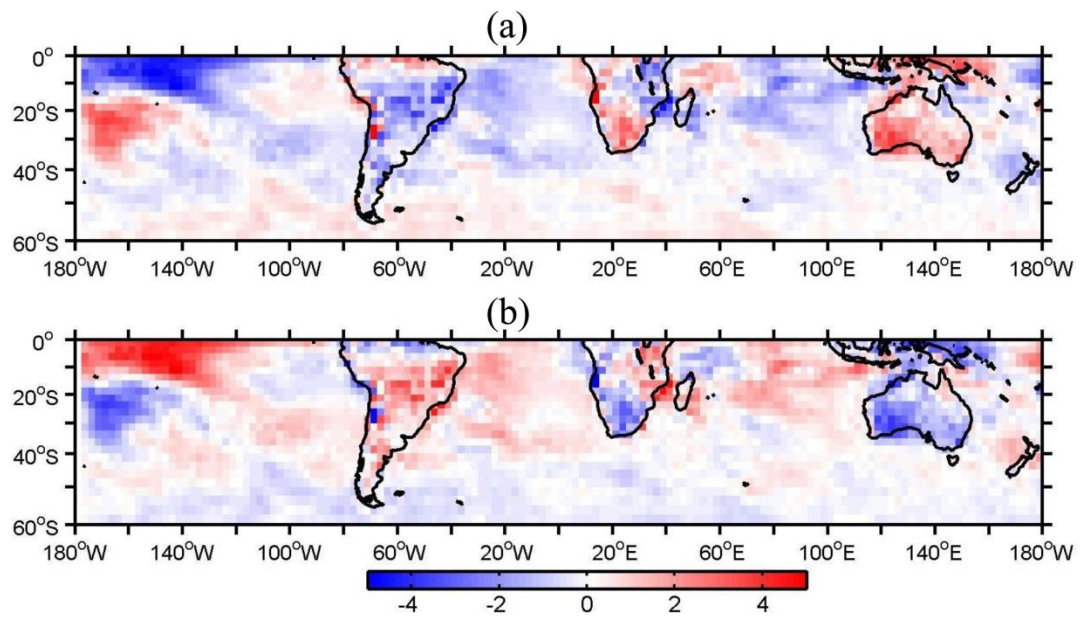
498

499

500

501

502



503

504 | Figure 5. Climatological OLR anomalies ( $\text{W m}^{-2}$ ) during (a) 1979-1999 and (b) 2000-2020, with  
 505 respect to the 42-year climatology over the 1979-2020 period.

506

507

508

509

510

511

512

513

514

515

516

517

518

519

520

521

522

523

524

525

526

527

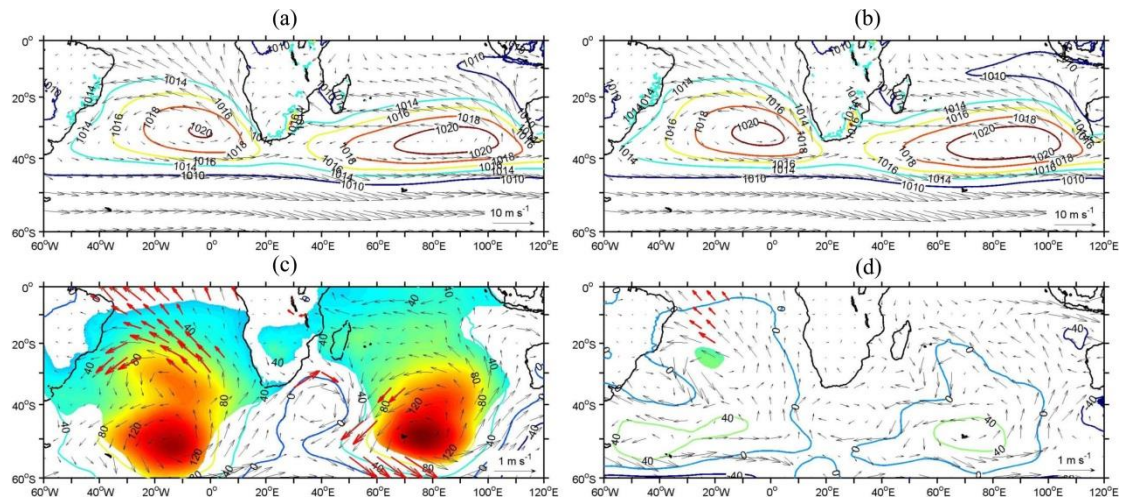
528

529

530

531





532

533

534

Figure 6. Climatological mean sea level pressure (MSLP, in hPa) and 10-m wind field (vector)

535

over the periods of (a) 1979-1999 and (b) 2000-2020, and regression maps of MSLP (in Pa) and

536

10-m wind field (vector) onto the summertime SAOD index over the periods of (c) 1979-1999

537

and (d) 2000-2020. Shaded regions and red vectors indicate above 95% confidence level.

538

539

540

541

542

543

544

545

546

547

548

549

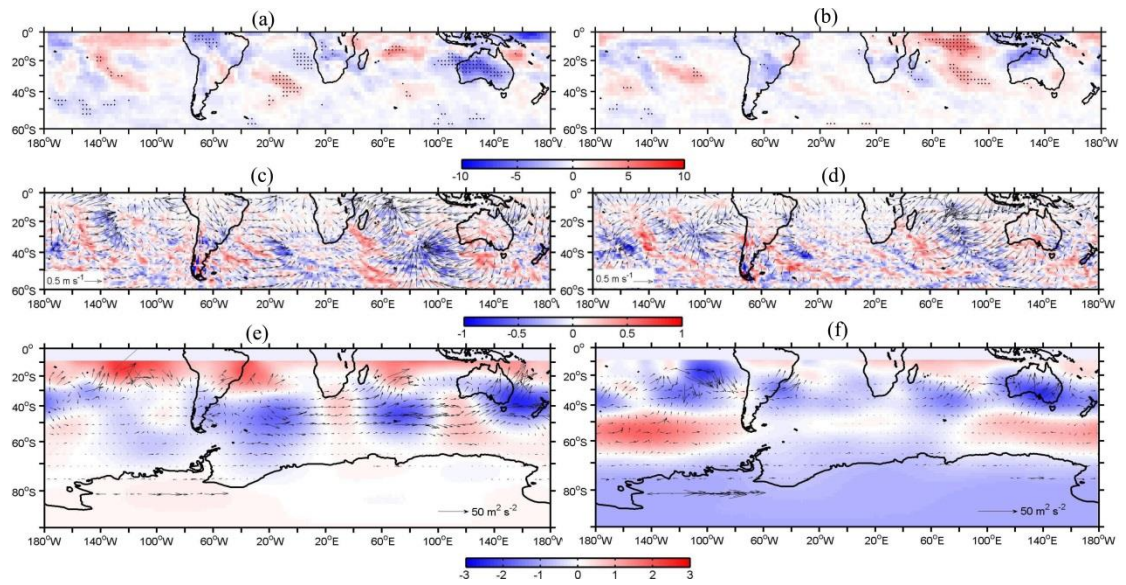
550

551

552

553

554



555

556 Figure 7. Regression maps of- (a), (b) ~~outgoing longwave radiation (OLR)~~ ( $\text{W m}^{-2}$ ), (c), (d)  
 557 ~~Rossby wave source (RWS)~~ ( $10^{-10} \text{ s}^{-2}$ ) and 200-hPa divergent wind (vector), (e), (f) ~~WAF wave~~  
 558 ~~activity flux~~ (vector) and streamfunction ( $\text{m}^2 \text{ s}^{-1}$ ) onto the summertime SIOD index over the  
 559 1979-1999 period (a), (c), (e) and the 2000-2020 period (b), (d), (f).

560

561

562

563

564

565

566

567

568

569

570

571

572

573

574

575

576

577

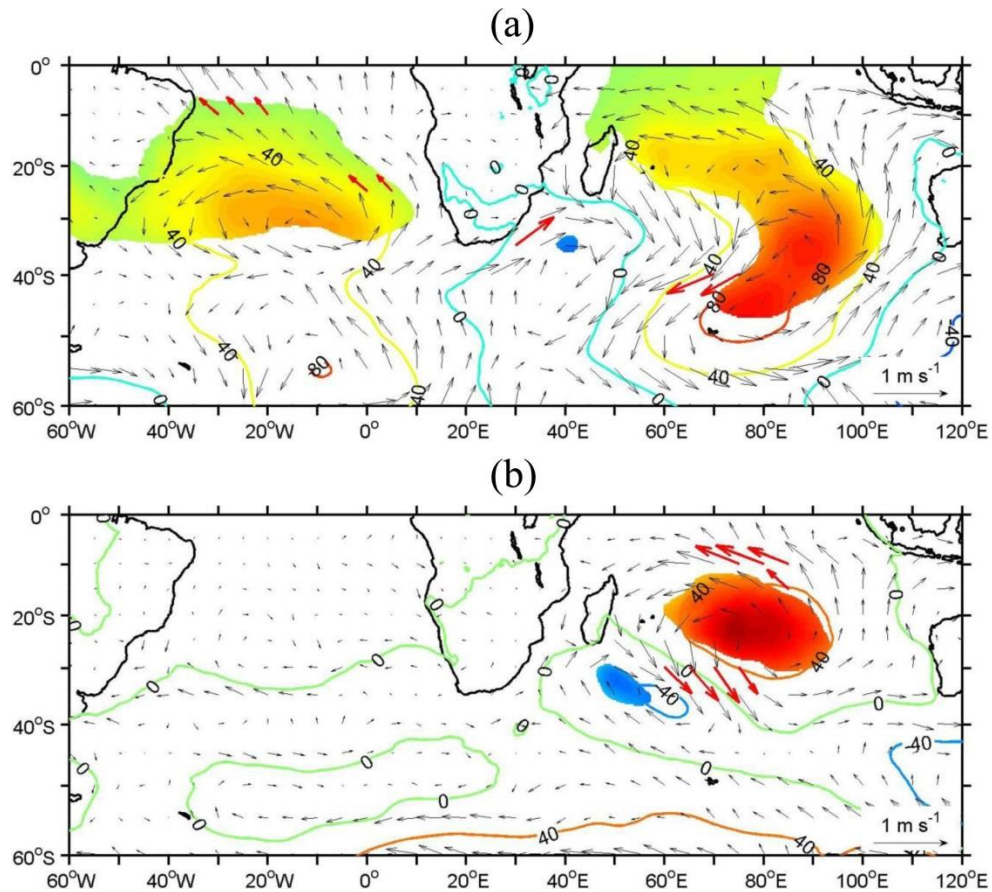
578

579

580

581





582

583 Figure 8. Regression maps of MSLP (in Pa) and 10-m wind field (vector) onto the summertime  
 584 SIOD index over the periods of (a) 1979-1999 and (b) 2000-2020. Shaded regions and red vectors  
 585 indicate above 95% confidence level.

586

587

588

589

590

591

592

593